Boron nitride embedded in chitosan hydrogel as a hydrophobic, promising metal-free, sustainable antibacterial material

Nisrine Hammi, M. Kedzierska, N. Wronska, N. Katir, Jeremy Dhainaut, Sebastien Royer, K. Lisowska, M. Bryszewska, K. Milowska, A. El Kadib

Materials Advances

ROYAL SOCIETY OF CHEMISTRY

PAPER

View Article Online
View Journal | View Issue

Check for updates

Cite this: *Mater. Adv.*, 2023, 4, 5191

Boron nitride embedded in chitosan hydrogel as a hydrophobic, promising metal-free, sustainable antibacterial material†

Nisrine Hammi,[ab] Marta Kędzierska,[c] Natalia Wrońska,[d] Nadia Katir,[a] Jeremy Dhainaut,[b] Sebastien Royer,[b] Katarzyna Lisowska,[d] Maria Bryszewska,[c] Katarzyna Miłowska[c] and Abdelkrim El Kadib *[a]

Received 21st July 2023,
Accepted 18th September 2023

DOI: 10.1039/d3ma00445g

rsc.li/materials-advances

Evaporation-induced co-assembly of boron nitride-exfoliated chitosan hydrogel provides micrometer-thick boron nitride-filled chitosan nanocomposite films. Owing to the favorable interfacial interaction of NH_2 belonging to chitosan and boron center in boron nitride (BN) sheets, a loading of up to 60 wt% of boron nitride could be entrapped inside, without compromising the film quality or its flexibility. Notably, increasing boron nitride loading alters the wettability of the resulting films and improves its mechanical and thermal properties. Enhanced biological response (*e.g.*, antibacterial properties) also correlates with the entrapped amount of boron nitride, which highlights the potential use of the latter as metal-free, antibacterial surface coating materials.

1. Introduction

The urgent need for more efficient antibacterial and antiviral materials is driven by the widespread of bacteria and virus and the emergence of antibiotic-resistant organisms.[1] Most antibacterial and antiviral materials are based on metal and metal oxide-containing nanomaterials.[1b,2] Popular examples are silver nanoparticles, zinc oxide, copper oxide, and titanium dioxide.[3] While they are proven to be effective, the implementation of these metal-based nanomaterials is fraught with challenges, such as high toxicity, that hinders daily use in places hosting vulnerable persons (*e.g.*, hospitals, nursing home, and kindergarten)[4] and their possible accumulation in the environment raises concerns.[5] Additional drawback lies on the poor understanding of the exact nature of the antibacterial site (nanoparticles *versus* clusters and/or ionic atoms), rendering it difficult to establishment a clear correlation between the structure and biological activity.[6] Alternatively, synthetic polymers and reactive organic building-blocks,[7] particularly those featuring ammonium in their side chains, display promising biological response with additional assets of being structurally well-defined, fully degradable, and less toxic.[8] Unfortunately, tailorable functional polymeric architectures required for such purpose are not often easily accessible, with their development being impeded by the dearth of efficient synthetic methods. In most optimistic scenarios, the cost associated with the synthesis of potential derivatives overwhelms to a major extent their benefits.[9]

An alternative solution to these man-made ammonium-based polymers could be the direct use of naturally occurring biomass and more preferably those discarded as bio-waste to avoid additional synthetic chemistry.[10] Chitosan meets these requirements owing to the abundance of its source (chitin) for which trivial deacetylation affords an auspicious polymeric backbone of linked 2-amino-2-deoxy-D-glucan and 2-acetamidodeoxy-D-glucan.[11] Chitosan is the sole accessible cationic natural polymer, making its interaction with negatively charged species highly favorable. Chitosan also coordinates Lewis acid metals and clusters,[12] allowing its use for metal sequestration and heterogeneous catalysis.[13] Besides, chitosan can be handled on demand and shaped as transparent film with controllable thickness.[14] This flexibility in configuring chitosan substructure[14,15] avoids the tyranny of shaping the final material into a suitable end use device, a step that is recognized as very challenging to derive laboratory-successful materials for the market.

[a] *Euromed Research Center, Engineering Division, Euro-Med University of Fes (UEMF), Route de Meknes, Rond-point de Bensouda, 30070, Fès, Morocco. E-mail: a.elkadib@ueuromed.org*
[b] *Univ. Lille, CNRS, Centrale Lille, Univ. Artois, UMR 8181-UCCS-Unité de Catalyse et Chimie du Solide, F-59000 Lille, France*
[c] *Department of General Biophysics, Faculty of Biology and Environmental Protection, University of Lodz, 141/143 Pomorska Street, 90-236 Lodz, Poland*
[d] *Department of Industrial Microbiology and Biotechnology, Faculty of Biology and Environmental Protection, University of Lodz, 12/16 Banacha Street, 90-236 Lodz, Poland*

† Electronic supplementary information (ESI) available. See DOI: https://doi.org/10.1039/d3ma00445g

Though suffering from low chemical, thermal, and mechanical stability, some of these properties can be improved by associating chitosan with a variety of nano-sized objects, including hydroxyapatite, carbon derivatives (graphene and carbon nanotubes), clay, metal and metal oxide nanoparticles, and cellulose-based micro- and nanocrystals.[16] These materials have been used for antibacterial purposes, with a remarkable synergistic contribution of the filler to their biological response in few cases. Unfortunately, some of these fillers lead simultaneously to the hemolysis of human red blood cells, low biocompatibility, and high cytotoxicity, making the exploration of new and innovative filler candidates necessary.

Hitherto marginally explored for the above-mentioned purposes, boron nitride (BN) displays many exciting features that could open more possibilities as metal-free antibacterial materials. Boron nitride is structurally similar to graphene and carbon nanotubes, with additional advantages of being highly polarized and sensitive to radicals. Besides, early studies have claimed that BN nanotubes (NTs) and hexagonal BN are more cytocompatible than their carbon counterparts *in vitro* and *in vivo*.[17]

While graphene and carbon nanotubes have been the focus of extensive biological studies, boron nitride seems to be forgotten, in spite of the above cited advantages.[18] We recently initiated a research program revolving around the use of chitosan marine waste for the preparation of sustainable bio-based packaging and antibacterial materials.[19] We have explored the holistic association of chitosan with a variety of sophisticated objects including single and mixed metal oxides,[20] lamellar and tubular clay nanoparticles,[21] surface-modified graphene oxide,[22] metal–organic framework,[23] and phosphorylated cellulose nanocrystals.[24] Prompted by the inherent properties of boron nitride, we herein embarked to investigate the possible embedding of boron nitride in chitosan films through evaporation-induced assembly of their colloidal solution to conceive radical-sensitive packaging films. We have specifically assessed the effect of BN loading on the mechanical, thermal, and chemical properties of the resulting boron nitride-filled chitosan films (**CS-BN$_x$-*f***). We have also evaluated some of their biological properties, including their antibacterial activity against *Escherichia coli* and *Staphylococcus aureus*, hemolysis, and cytotoxicity.

2. Experimental

2.1 Materials and reagents

Commercially available reagents and solvents were purchased from Across and Sigma-Aldrich (St. Louis, MO, USA). Chitosan of medium molecular weight (viscosity: 200–800 cps and a deacetylation degree of 75–85%) was purchased from Sigma-Aldrich (Hamburg, Germany). h-BN (CAS number 10043-11-5) was purchased from Sigma-Aldrich.

2.2 Preparation of boron nitride-filled chitosan nanocomposite films

A total of 0.1 g chitosan was dissolved in 8 mL aqueous acetic acid (1% v/v). The boron nitride suspension was prepared by dispersing a proper amount of boron nitride in hot water with sonication for 1 h and then gradually added to the chitosan solution, followed by stirring at ambient temperature for 24 h. Boron nitride-filled chitosan solutions were subsequently poured into a plastic Petri dish and dried under room temperature to form films. For comparison, pure chitosan films were also prepared in the same way but without the addition of boron nitride. The obtained films were denoted as **CS-BN$_x$-*f*** (x refers to the BN content: x = 1, 3, 5, 10, 30, 40, and 60 wt%).

2.3 Characterization

Fourier-transform infrared spectra (ATR FT-IR) were obtained with a PerkinElmer Spectrum 100FT-IR spectrometer on neat samples. X-Ray diffraction (XRD) was performed using a Bruker X-ray AXS D8 Advance diffractometer in Bragg–Brentano configuration and equipped with a LynxEye Super Speed detector. XRD patterns were recorded with Cu Kα radiation (λ = 0.154 nm, 40 kV, 30 mA) in the 10–80° 2θ range with a 0.05° 2θ step. Scanning transmission electron microscopy–energy dispersive X-ray spectroscopy (STEM-EDX) was conducted using a FEG TEM/STEM system (Titan Themis FEI) operated at 300 kV. The microscope was equipped with a monochromator, a super-X windowless four-quadrant silicon drift detector (SDD) for the STEM-EDX mapping, and a probe Cs corrector allowing spatial resolution of about 65 pm. Thermogravimetric analyses (TGA) under air were done with a thermal analyzer instrument Q500 in the range of 25–900 °C with the ramp of 5 °C min^{-1}. Contact angle measurements were recorded using a dynamic contact angle meter (KRUSS GmbH Easy Drop, Kruss GmbH, Hamburg, Germany) equipped with a charge-coupled device camera and using an image capture program employing scat software (VCA Optima, AST Products, Billerica, MA, USA). The cut film (3 cm × 3 cm) was fixed on the top of a dynamic support. A droplet (3 μL) was placed on the film surface, and the change in the contact angles was treated by the software (VCA Optima, AST Products, Billerica, MA, USA) of the apparatus. Each measurement was repeated four times, and their average was considered. Tensile tests of the long films were performed on an Instron testing machine, Model 4466. The samples were drawn at a crosshead speed of 10 mm min^{-1} using a 100 N load cell at room temperature. A single bundle of films was partially locked at its ends in a stiff cardboard paper, giving a gauge length of 25 mm. Each sample diameter was calculated from an average of three values using a Mitutoyo electronic micrometer.

2.4 Biological activity of boron nitride-filled chitosan nanocomposite films

2.4.1 Antimicrobial Activity of CS-BNx-*f*. The evaluation of the antibacterial activity of boron nitride-filled chitosan films was done using the Japanese Industrial Standard JIS Z 2801 : 2000 (with modifications). Bacteria were cultured on Luria–Bertani (LB) medium at 37 °C on a rotary shaker. After the incubation, the test inoculum of *S. aureus* and *E. coli*, containing 1 × 105 colony-forming units (CFU per mL) in 500-fold diluted LB medium, was prepared. Next, the bacterial suspension was applied to the tested films of 1 cm × 1 cm.

Native, unmodified chitosan films were analyzed as a control sample. After dripping the suspension of selected bacteria on the tested materials (chitosan films), each sample was covered with a sterile film (1 cm × 1 cm). Next, the samples were incubated in the moist chamber for 24 h at 37 °C. After incubation, the samples were put in the sterile tube containing phosphate buffer and vortexed. After that, the films were removed from the tubes, and with the remaining solution, a serial dilution was performed in phosphate buffer. Out of each dilution, 100 μL bacterial suspension was seeded on agar plates and incubated for 24 h at 37 °C. Next, the viable cells of *S. aureus* or *E. coli* were counted. Each type of film was tested in triplicate and analyzed individually in three independent experiments.

2.4.2 Hemolysis assay. Blood from healthy donors was obtained from the Regional Blood Donation and Blood Treatment Center in Lodz (Poland). Erythrocytes were separated from blood plasma and leukocytes by centrifugation (3000 rpm, 10 min) at 4 °C and washed three times with PBS (phosphate buffered saline; pH = 7.4). Erythrocytes were used immediately after isolation. To study the effect of chitosan–boron nitride composites on erythrocyte stability, red blood cells (RBCs) suspended in PBS to a final hematocrit (HTC) of 10% were treated with different modification of chitosan–boron nitride composites in the form of squares with dimensions 0.5 cm × 0.5 cm. RBCs suspended in PBS (without composites) were used as a control. The erythrocyte suspensions were incubated with squares of chitosan–boron nitride composites at 37 °C for 3 and 24 h. Samples were centrifuged at 3000 rpm for 10 min, and the absorbance of the supernatant was measured spectrophotometrically at 540 nm. The percentage of hemolysis was determined on the basis of the hemoglobin (Hb) released into the supernatants and calculated using the following formula

$$\%\ \text{Hemolysis} = A_s/A_c \times 100\%$$

where A_s represents the absorbance of the sample A_c represents the absorbance of the positive control (100% hemolysis).

2.4.3 Adsorption of hemoglobin (Hb). The experiment was carried out to investigate whether chitosan–boron nitride composites adsorb hemoglobin from the environment. Chitosan–boron nitride squares with dimensions of 0.5 cm × 0.5 cm were added to hemoglobin solutions. Samples were incubated in incubator at 37 °C for 3 or 24 h. After this time, the samples were centrifuged, and the absorbance of hemoglobin was measured at a wavelength of 540 nm. The percentage of hemoglobin adsorption was calculated from the formula

$$\text{Adsorption of Hb} = 100\% - (A_s/A_c \times 100\%)$$

where A_s is the absorbance of the sample containing the chitosan–alginate composites A_c is the absorbance of the control (hemoglobin without chitosan–boron nitride).

2.4.4 ABTS radical scavenging assay. The free radical scavenging activity of the films was determined by ABTS radical cation decolorization assay. ABTS and potassium persulfate were dissolved in distilled water to a final concentration of 7 mM and 2.45, mM respectively. These two solutions were mixed and the mixture allowed to stand in the dark at room temperature for 16 h before use in order to produce ABTS radical ($ABTS^{\bullet+}$). For the study, $ABTS^{\bullet+}$ solution was diluted with distilled water to obtain an absorbance of 0.7–0.9 at 734 nm. Film squares (0.5 cm × 0.5 cm) were added to $ABTS^{\bullet+}$ solution and incubated for 15 and 30 min. After incubation, the absorbance of the solution was measured spectrophotometrically (Jasco V-650, Jasco International Co., Osaka, Japan). An appropriate solvent blank was run in each assay. All the measurements were carried out at least three times. Percent inhibition of absorbance (scavenging effect) at 734 nm was calculated using the formula

$$\%\ \text{inhibition} = (A_0 - A)/A_0 * 100\%$$

where A_0 represents the absorbance of control (ABTS) at 734 nm A represents the absorbance of the sample (ABTS after incubation with films) at 734 nm.

3. Results and discussion

3.1 Preparation and characterization of boron nitride-filled chitosan films (CS-BNx-f)

As depicted in Scheme 1, nanocomposite films were prepared starting from water-soluble chitosan solution mixed with a solution of dispersed boron nitride (h-BN) of known weight concentration. The resulting solution was cast onto a clean Petri dish for 24 h until the total evaporation of the solvent. Whatever the amount of h-BN engaged in the initial solution (from 1 wt% to 60 wt%, final dry weight), homogenous, stable, and flexible **CS-BN$_x$-*f*** films were obtained, as illustrated in Scheme 1c. The shift from transparent to opaque white films reflects the increased amounts of the filler in the dry composites. The successful entrapment of such a large loading of boron nitride, up to 60 wt%, without compromising the film-forming properties of chitosan or its flexibility could be rooted in the strong interfacial interaction occurring between the filler and the polymer backbone. Considering the highest affinity of NH_2 to boron through base-to-acid coordination ($NH_2 \rightarrow B$), it is likely that a similar scenario occurs between the pendant amino groups of chitosan and boron atoms located on the flat sheets, which provide the driving force to disperse the inorganic filler even at high loading. In support of these assumptions, fast sedimentation occurs for native h-BN dispersed in aqueous medium [5 mg in 12 mL of H_2O] after 24 h while the CS-BN mixture stays stable for an extended time of at least seven days (Scheme 1d).

The FTIR spectra of **CS-BN$_x$-*f*** shows the fingerprint of both chitosan and h-BN (Fig. S1, ESI†). All the composite films show typical absorption peaks of chitosan, namely, the amine band (NH_2) at 1568 cm^{-1} and the carbonyl band (C═O–NHMe) at 1643 cm^{-1}.[25] The strong signature of h-BN at 762 cm^{-1}, attributed to B–N stretching, was present in all the **CS-BN$_x$-*f*** composite films, thus bringing a firm evidence for the incorporation of boron nitride inside the film-forming chitosan

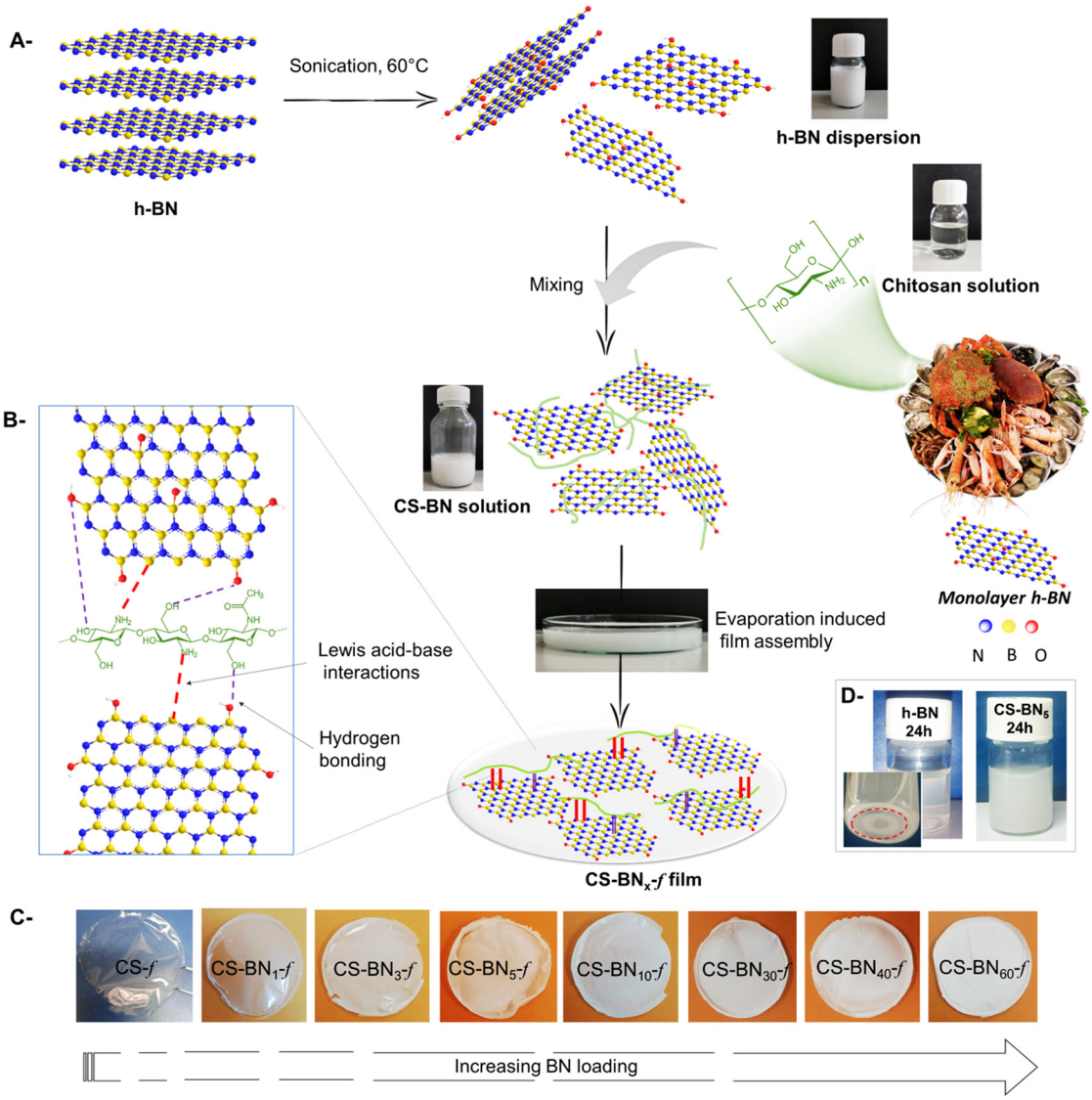

Scheme 1 (a) Illustration of the multistep preparation procedure for boron nitride-embedded chitosan hydrogels. (b) Chemical structure and interfacial interaction of chitosan and boron nitride. (c) The as-prepared hybrid films (denoted as **CS-BN$_x$-*f***) with increasing BN amount. Left to right: 0, 1, 3, 5, 10, 30, 40, and 60 wt%. (d) Digital photos of h-BN and **CS-BN$_5$** acidic-aqueous solution after 24 h.

network.[26] A significant increase in the intensity of the two stretching bonds of BN at 1309 cm^{-1} and 762 cm^{-1} occurs with increasing amount of BN engaged in the initial mixture. We have also noticed a minor shift of the two characteristic vibrations of chitosan (C═O–NH and NH$_2$) with respect to those in **CS-BN$_x$-*f***, as illustrated in Fig. S1 (ESI†). These variations suggest the occurrence of strong interfacial interactions between the two components, which seems in agreement with the long-term stability of exfoliated boron nitride/chitosan colloidal solution.[21a,23]

The XRD diffraction peaks of **CS-BN$_x$-*f*** films show sharp and well-resolved crystalline peaks that match the pristine structure of hexagonal boron nitride (Fig. S2, ESI†). This is in contrast to native chitosan structure, which exhibits only a broad amorphous peak at 20.4°.[25,27] The two sharp peaks observed at 2θ values of 26° and 55° are respectively attributed to the [002] and [004] crystallographic planes of h-BN, and the *d*-spacing value of the nanoparticles calculated for the peak at 2θ value of 26.7° was found to be 0.33 nm. Additionally, the intensity of the peak at 26.7° increases with increasing amount of BN loaded inside the **CS-BN$_x$-*f*** films, suggesting that boron nitride particulates preserve their inherent crystallinity inside of the film-forming network even at high concentrations of BN nanoparticles.[28]

The morphology of native chitosan films and its analogues **CS-BN$_x$-*f*** was next investigated using scanning electron microscopy (SEM), as shown in Fig. 1 and Fig. S4 (ESI†). The surface of the native chitosan film was smooth and regular without appreciable cracks (Fig. S4a, ESI†), while that of **CS-BN$_1$-*f***, **CS-BN$_5$-*f***, **CS-BN$_{10}$-*f***, and **CS-BN$_{30}$-*f*** showed a rough surface, with the highest fraction of h-BN being dispersed in the film and a very small amount of h-BN aggregates (Fig. S4b, ESI†). The roughness of the surface can be moreover confirmed by

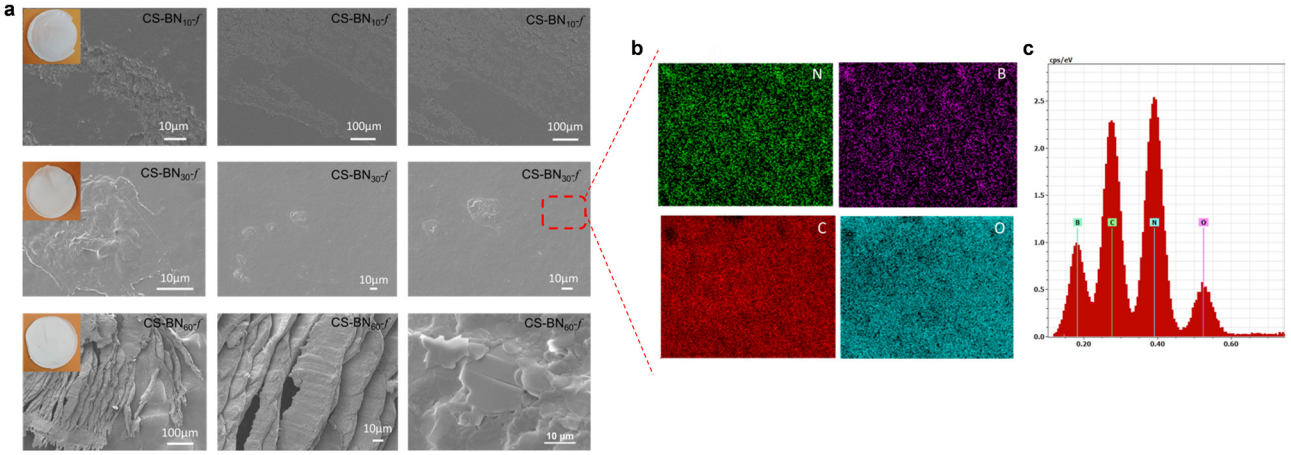

Fig. 1 Microstructural investigation of boron nitride-filled chitosan hydrogels. (a) SEM images of: **CS-BN$_{10}$-*f***, **CS-BN$_{30}$-*f***, and **CS-BN$_{60}$-*f*** and onset (the corresponding digital photos for each material); (b) Mapping the location of nitrogen, boron, carbon, and oxygen through SEM/EDX analysis; (c) Energy dispersive X-ray diffraction spectra showing the abundance of boron, carbon, nitrogen, and oxygen.

comparing the thickness of the films, with the native chitosan being the least thick (6 μm) while that of the most loaded **CS-BN$_{60}$-*f*** was 23 μm thicker (Table S5, ESI†).

Elemental mapping analysis undertaken for **CS-BN$_{30}$-*f*** revealed the uniform presence of boron, nitrogen, carbon, and oxygen within the network (Fig. 1b and c). The homogeneous distribution of BN inside the films was reached through successful dispersion and exfoliation of the filler inside, as previously commented. When the loading of BN nanolayers was further increased as in the case of **CS-BN$_{60}$-*f***, the microstructure of aligned BN nanoflakes becomes visible, indicating that the structure-directing assembly of BN particulates caused by their mutual interaction with the functionalities of the chitosan framework.

Improved thermal stability was noticed for the **CS-BN$_x$-*f*** films with increasing filler amount from 1 to 60 wt% compared to the native chitosan films (Fig. 2a and Fig. S3, ESI†). The half weight decomposition temperature provides valuable information about the thermal stability of the newly prepared films. Native chitosan exhibits a T_{50} of 338 °C, which is the lowest temperature within the series, while **CS-BN$_{60}$-*f*** displays a T_{50} of 495 °C, with the most delayed half weight degradation among the films. On the other hand, a complete decomposition was experienced for chitosan at 700 °C; a significant char residue was observed in case of the **CS-BN$_x$-*f*** films, which correlates well with the amount of BN engaged in the initial solution (Table S5, ESI†). No weight loss could be observed for native boron nitride due to its high thermal stability. Obviously, the entrapment of BN inside the films delays the polymer degradation and improves its thermal resistance, which open a new channel of possibilities as sustainable flame-retardant polymeric materials.[29]

Contact angle measurements show a dramatic change in the surface wettability of **CS-BN$_x$-*f*** nanocomposites compared to the pristine chitosan film (Fig. 2b). As the amount of the filler increases, the water contact angle follows the same trend, reaching 102.9° for **CS-BN$_{60}$-*f*** compared to 67.4° for native chitosan film. This corresponds to a significant shift of the $\Delta\theta$ value equal to 35°. The increased surface roughness in **CS-BN$_x$-*f*** associated with the rigidity of the sheets that hinder the hydrogen-bonding network of the polysaccharides from being exposed to the surface reduces the inherent hydrophilicity of the initial film and switches the surface properties to water repellent and hydrophobic,[22a] which render **CS-BN$_x$-*f*** nanocomposites more adaptable to moisture-resistant applications.

Fig. 2c shows the tensile stress *vs.* strain curves for native chitosan CS and its **CS-BN$_x$-*f*** congeners. During the deformation of the films, three phases were observed on the stress–strain curves, namely, the elastic region, the stable stage (plateau), and the final stage where the stress decreased rapidly.[30] At the beginning of the loading process, the stress–strain curve is nonlinear, which is a typical feature of soft polymer materials.[31] Fig. 2d displays the tensile strength and elongation at break. The composite film containing 30 wt% BN layers (**CS-BN$_{30}$-*f***) exhibited the highest tensile strength of about 119 MPa and a maximum elongation at break of 30%. These two respective values present an improvement of 26% and 7% to those recorded for neat chitosan film. This record outperforms the ones reached using graphene oxide CS-GO-*f* (60 MPa)[32] and phosphorylated cellulose nanocrystals CS@PN-CNC-*f* (53 MPa),[24] respectively. Besides, in most cases, an improvement in tensile strength has been often counterbalanced by a significant decrease in the elongation at break properties, which is not the case with **CS-BN$_{30}$-*f***. This unprecedented result indeed opens more possibilities for reinforcing chitosan-based nanocomoposites.[24] Impressively, **CS-BN$_{30}$-*f*** displayed the highest tensile strength among all boron nitride-filled polymer nanocomposites reported in the literature so far (Table S6, ESI†). **CS-BN$_{60}$-*f*** displayed the lowest tensile strength of 10 MPa and a brittle-like behavior because of the significant aggregation of BN layers through π–π stacking, as evidenced by SEM analysis. The presence of aggregated

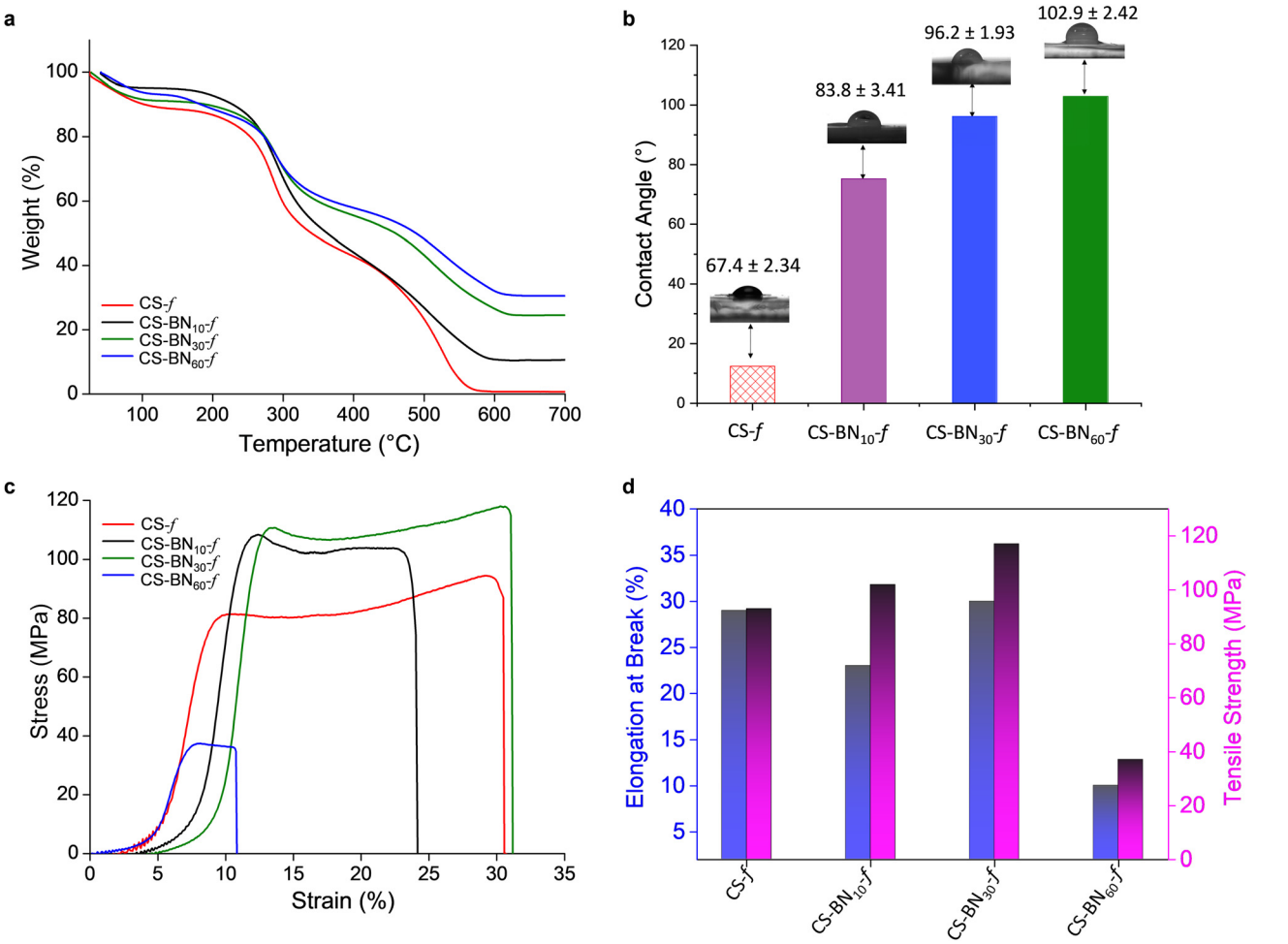

Fig. 2 Elucidating the impact of boron nitride loading on the key properties of BN-embedded chitosan hydrogels: (a) Thermogravimetric analysis; (b) contact angle measurement; (c) tensile stress–strain curves; and (d) tensile strength and elongation at break of **CS-*f***, **CS-BN$_{10}$-*f***, **CS-BN$_{30}$-*f***, and **CS-BN$_{60}$-*f*** films. Values are averaged based on four repeated tests.

microparticles and tactoides within the polymer network is known to worsen the mechanical properties of reinforced polymer-based nanocomposites.

3.2 Biological activity of CS-BN$_x$-*f* nanocomposites

For the biological activity, we intentionally focused on hydrogels containing a lower amount of boron nitride because of their suitability for packaging in terms of flexibility and transparency as well as the cost-effectiveness of the final material considering that chitosan bio-waste is cheaper compared to boron nitride. Besides, when the aqueous formulation was used as an antiseptic spray, optimally discrete and uniform coating could be obtained with a lower amount of boron nitride. We have consequently investigated the antibacterial activities of native chitosan **CS-*f*** and marginally-loaded **CS-BN$_x$-*f*** nanocomposites (*i.e.*, **CS-BN$_1$-*f***, **CS-BN$_3$-*f***, and **CS-BN$_5$-*f***) against *Escherichia coli* and *Staphylococcus aureus* (Fig. 3a). Native **CS-*f*** used as a control did not inhibit the growth of *E. coli* or *S. aureus*. The low antibacterial activity of chitosan once shaped as films is already documented and mainly attributed to the inaccessibility of NH_2 groups on the flattened surface.[20,33] In turn, **CS-BN$_1$-*f***, **CS-BN$_3$-*f***, and **CS-BN$_5$-*f*** displayed good antibacterial activities against *E. coli* and even nearly excellent activity against *S. aureus*. The antibacterial activity increased with increasing amounts of BN nanolayers in the film: **CS-BN$_5$-*f*** > **CS-BN$_3$-*f*** > **CS-BN$_1$-*f***. A similar trend was observed for both Gram-positive and Gram-negative bacteria. These results are very interesting given that in the literature, appreciable antibacterial activity was noticed only after filler conjugation when cellulose and graphene oxide are entrapped in chitosan hydrogel films.[22b,24] Herein, commercially available boron nitride was used as such without the additional step of functionalization that could add cost and interfere with the biocompatibility.

Common claims in the literature focused primarily on the cationic groups of chitosan (either NH_2 or ammonium) as responsible sites that interact with negatively charged components present on the bacterial surface, leading to membrane disturbance.[34] However, the also literature highlighted the role of the surface wettability, with hydrophobic materials being more efficient to eradicate bacteria.[35] This parameter appears

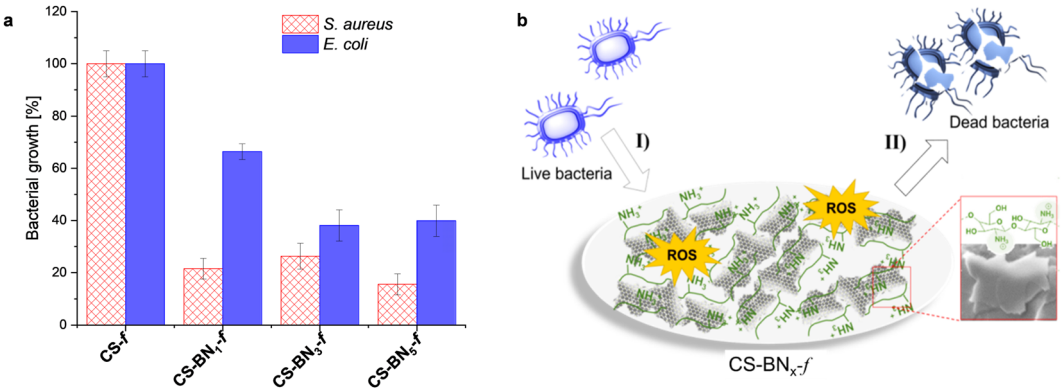

Fig. 3 (a) Antibacterial activity of the resulting nanocomposite films: Inhibition (%) of *Escherichia coli* and *Staphylococcus aureus* after 24 h incubation. (b) Plausible mechanism illustrating the interplay of the **CS-BN$_x$-*f*** nanocomposite with bacteria.

in concordance with the wettability enhancement of chitosan films noticed with the increased loading of boron nitride. A close look at the literature shows the importance of the partnered polymer, with no significant decrease in bacterial density being observed for Pluronic P123, Pluronic F127, and ammonium oleate-coated boron nitride, while polyethylenimine-coated boron nitride resulted in significant antibacterial activity.[36]

We indeed tentatively propose that the bacteria are damaged by the flattened BN surface, which leads to the death of cells.[37] A suggested mechanism of the **CS-BN$_1$-*f*** films interacting with the bacterial cells is shown in Fig. 3b. The antimicrobial process concerns mainly two steps: first, the bacteria are attracted onto the surface of the **CS-BN$_x$-*f*** nanocomposite by the strong electrostatic interaction between the positive charge belonging to chitosan and the negative charge from the bacterial cell. Thereafter, on the one hand, BN nanoplates with numerous sharp edges on the surface penetrate and disrupt the cell membranes of the bacteria and cause its inactivation.[17b,37] On the other hand, the possible existence of unsaturated B atoms (B radicals) at the BN nanoplates edges could trigger the generation of ROS, leading to cell death.[38] However, as will be commented later, these materials also display interesting antioxidant activity, which could attenuate the damaging effects of ROS and delay many events that contribute to cellular aging.[39]

The hemolysis of human erythrocytes was evaluated by measuring the hemoglobin content after incubating the cells with **CS-BN$_x$-*f*** films for 3 and 24 h. The hemolysis results for all **CS-BN$_x$-*f*** films are presented in Fig. 4a. While all the **CS-BN$_x$-*f*** films induced hemolysis upon initial inspection, the hemolysis percentage did not exceed 7% after incubation for 3 h. After 24 h of incubation, the percentage of hemolysis increased up to 8.5%. The hemolysis rate also increased with increasing concentrations of BN nanolayers (from 1 wt% to 3 wt%) in the **CS-BN$_x$-*f*** composites. However, a further increase in the BN nanolayer contents up to 5 wt% led to a slight decrease in the hemolysis rate, which could be attributed to the higher hydrophobicity and reduced affinity of bacterial cells.[40] Notably, all the **CS-BN$_x$-*f*** films demonstrated lower hemolytic activity compared to the already reported chitosan films filled with graphene oxide, CS-GO (7–7.5%), and those filled with nanocellulose (10–16%).[22b,24,32] As hemolysis was not dependent on the incubation time, we investigated the possible hemoglobin adsorption on the surface of the films (Fig. 4b). It is widely accepted that BN nanosheets adhere to the cell membrane, disrupting the membrane integrity and causing membrane leakage.[41] However, contact angle measurements

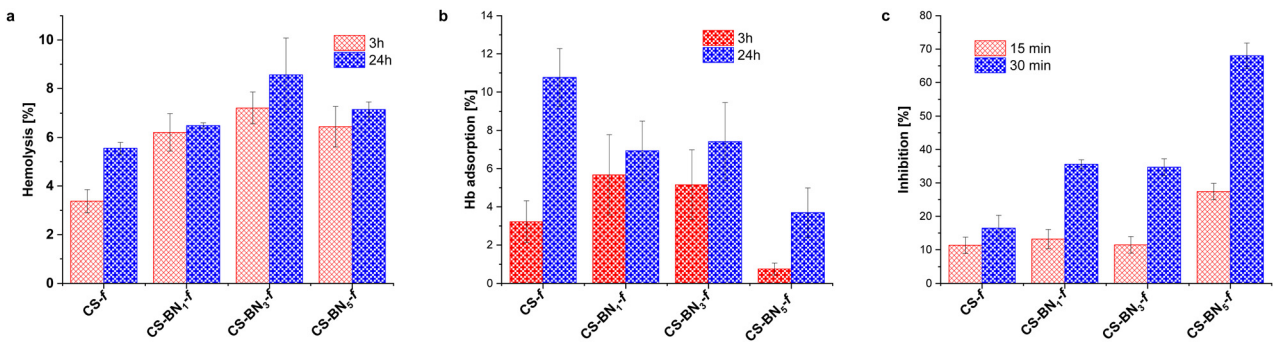

Fig. 4 (a) Hemolysis of erythrocytes after incubation with **CS-BN$_x$-*f***; (b) hemoglobin adsorption on the surface of boron nitride-embedded chitosan hydrogels; and (c) ABTS radical scavenging activity of **CS-BN$_x$-*f***.

revealed that the BN nanolayers increased the hydrophobicity of the chitosan film, which may reduce the cell affinity to **CS-BN$_x$-*f***, thus decreasing the possibility of cell-killing. Therefore, the percentage of hemolysis after 24 h may not reflect real hemolytic activity but rather the accumulation of hemoglobin on the surface of boron nitride composites.

Next, the antioxidant activity of the **CS-BN$_x$-*f*** films was assessed using the ABTS method, and the results showed a noteworthy increase in the antioxidant capacity of the films as the BN loading (1 wt%, 3 wt%, 5 wt%) increased, compared to the pure chitosan film. These findings are in line with the previously reported antioxidant activity of both BN and chitosan, as documented in the literature.[28a,42]

4. Conclusions

Herein, we describe a novel approach for the assembly of boron nitride-chitosan hydrogels through evaporation-induced co-assembly. Regardless of the amount of boron nitride, the resulting combination provides homogeneous, flexible, stable, and crack-free nanocomposite films. The strong interfacial interaction between the filler and the polymer backbone provides the driving force for the successful entrapment of up to 60 wt% of boron nitride without compromising the film-forming properties of the network or its flexibility. Increasing the amount of boron nitride significantly improves the thermal and mechanical properties along with significant alteration of the surface wettability. While native chitosan film was devoid of appreciable antibacterial activity, introducing a tiny amount of boron nitride (1 wt% to 5 wt%) imparted **CS-BN$_x$-*f*** nanocomposites with good antibacterial activities against Gram positive *Staphylococcus aureus* and Gram negative *Escherichia coli*. A slight variation in hemolysis was noticed with the addition of BN nanolayers while a significant increase in the antioxidant capacity of **CS-BN$_x$-*f*** nanocomposites was recorded with increasing BN loading. The results suggest the potential application of boron nitride-filled chitosan nanocomposites for the development of metal-free, antibacterial surface-coating materials.

Conflicts of interest

There are no conflicts to declare.

Acknowledgements

AEK thanks l'Académie Hassan II des Sciences et Technique for funding ''Nano-Bio-Mat'' project. NH thanks UEMF for the Scholarship. The Chevreul Institute is thanked for its help in the development of this work through the ARCHI-CM project supported by the ''Ministere de l'Enseignement Superieur de la Recherche et de l'Innovation'', the region ''Hauts-de-France'', the ERDF program of the European Union and the ''Metropole Europeenne de Lille. Adeline MARIN is warmly acknowledged for the mechanical testing.

References

1 (*a*) J. Fu, T. Liu, S. S. Binte Touhid, F. Fu and X. Liu, *ACS Nano*, 2023, **17**, 1739–1763; (*b*) S. M. Imani, L. Ladouceur, T. Marshall, R. Maclachlan, L. Soleymani and T. F. Didar, *ACS Nano*, 2020, **14**, 12341–12369.

2 (*a*) J. Hodek, V. Zajícová, I. Lovětinská-Šlamborová, I. Stibor, J. Müllerová and J. J. B. M. Weber, *BMC Microbiol.*, 2016, **16**, 1–12; (*b*) Y. C. Ong, S. Roy, P. C. Andrews and G. Gasser, *Chem. Rev.*, 2019, **119**, 730–796.

3 (*a*) F. Paladini, M. Pollini, A. Sannino and L. Ambrosio, *Biomacromolecules*, 2015, **16**, 1873–1885; (*b*) G. Reina, S. Peng, L. Jacquemin, A. F. Andrade and A. Bianco, *ACS Nano*, 2020, **14**, 9364–9388; (*c*) A. Rana, S. Pathak, D.-K. Lim, S.-K. Kim, R. Srivastava, S. N. Sharma and R. Verma, *ACS Appl. Nano Mater.*, 2023, **6**, 8106–8134; (*d*) M. L. Ermini and V. Voliani, *ACS Nano*, 2021, **15**, 6008–6029.

4 N. Karim, S. Afroj, K. Lloyd, L. C. Oaten, D. V. Andreeva, C. Carr, A. D. Farmery, I.-D. Kim and K. S. Novoselov, *ACS Nano*, 2020, **14**, 12313–12340.

5 V. Bhandari, S. Jose, P. Badanayak, A. Sankaran and V. Anandan, *Ind. Eng. Chem. Res.*, 2022, **61**, 86–101.

6 A. I. Ribeiro, A. M. Dias and A. Zille, *ACS Appl. Nano Mater.*, 2022, **5**, 3030–3064.

7 (*a*) S. Ladhari, N.-N. Vu, C. Boisvert, A. Saidi and P. Nguyen-Tri, *ACS Appl. Bio Mater.*, 2023, **6**, 1398–1430; (*b*) F. Khan, N. Tabassum, N. I. Bamunuarachchi and Y.-M. Kim, *J. Agric. Food Chem.*, 2022, **70**, 4817–4838; (*c*) F. Hui and C. Debiemme-Chouvy, *Biomacromolecules*, 2013, **14**, 585–601.

8 (*a*) M. Haktaniyan and M. Bradley, *Chem. Soc. Rev.*, 2022, **51**, 8584–8611; (*b*) Y. Lu, X. Xu and J. Li, *J. Mater. Chem. B*, 2023, **11**, 3338–3355; (*c*) A. Dong, Y.-J. Wang, Y. Gao, T. Gao and G. Gao, *Chem. Rev.*, 2017, **117**, 4806–4862; (*d*) E.-R. Kenawy, S. D. Worley and R. Broughton, *Biomacromolecules*, 2007, **8**, 1359–1384; (*e*) A. Jain, L. S. Duvvuri, S. Farah, N. Beyth, A. J. Domb and W. Khan, *Adv. Healthcare Mater.*, 2014, **3**, 1969–1985.

9 (*a*) B. H. Gan, J. Gaynord, S. M. Rowe, T. Deingruber and D. R. Spring, *Chem. Soc. Rev.*, 2021, **50**, 7820–7880; (*b*) A. S. Carlini, L. Adamiak and N. C. Gianneschi, *Macromolecules*, 2016, **49**, 4379–4394.

10 B. Ates, S. Koytepe, A. Ulu, C. Gurses and V. K. Thakur, *Chem. Rev.*, 2020, **120**, 9304–9362.

11 (*a*) N. Yan and X. Chen, *Nature*, 2015, **524**, 155–157; (*b*) X. Chen, H. Yang and N. Yan, *Chem. – Eur. J.*, 2016, **22**, 13402–13421.

12 (*a*) A. E. Kadib, K. Molvinger, M. Bousmina and D. Brunel, *J. Catal.*, 2010, **273**, 147–155; (*b*) A. El Kadib and M. Bousmina, *Chem. – Eur. J.*, 2012, **18**, 8264–8277; (*c*) A. El Kadib, A. Primo, K. Molvinger, M. Bousmina and D. Brunel, *Chem. – Eur. J.*, 2011, **17**, 7940–7946.

13 (*a*) B. Boumhidi, N. Katir, J. El Haskouri, K. Draoui and A. El Kadib, *New J. Chem.*, 2020, **44**, 14136–14144; (*b*) Á. Molnár, *Coord. Chem. Rev.*, 2019, **388**, 126–171; (*c*) A. El Kadib, *ChemSusChem*, 2015, **8**, 217–244.

14 S. Ladet, L. David and A. Domard, *Nature*, 2008, **452**, 76–79.
15 (*a*) A. El Kadib, *Chem. Rec.*, 2020, **20**, 753–772; (*b*) S. Takeshita, S. Zhao, W. J. Malfait and M. M. Koebel, *Angew. Chem., Int. Ed.*, 2021, **60**, 9828–9851.
16 (*a*) J. Li, X. Tian, T. Hua, J. Fu, M. Koo, W. Chan and T. Poon, *ACS Appl. Bio Mater.*, 2021, **4**, 4014–4038; (*b*) H. Wang, J. Qian and F. Ding, *J. Agric. Food Chem.*, 2018, **66**, 395–413; (*c*) L. Bonnaire, S. Sandra, T. Helgason, E. A. Decker, J. Weiss and D. J. McClements, *J. Agric. Food Chem.*, 2008, **56**, 3791–3797; (*d*) S. Kumar, A. Mukherjee and J. Dutta, *Trends Food Sci. Technol.*, 2020, **97**, 196–209; (*e*) J. Yu, D. Wang, N. Geetha, K. M. Khawar, S. Jogaiah and M. Mujtaba, *Carbohydr. Polym.*, 2021, **261**, 117904.
17 (*a*) S.-W. Xiong, P.-G. Fu, Q. Zou, L.-Y. Chen, M.-Y. Jiang, P. Zhang, Z.-G. Wang, L.-S. Cui, H. Guo and J.-G. Gai, *ACS Appl. Mater. Interfaces*, 2021, **13**, 196–206; (*b*) S. Pandit, K. Gaska, V. R. S. S. Mokkapati, S. Forsberg, M. Svensson, R. Kádár and I. Mijakovic, *RSC Adv.*, 2019, **9**, 33454–33459; (*c*) X. Chen, P. Wu, M. Rousseas, D. Okawa, Z. Gartner, A. Zettl and C. R. Bertozzi, *J. Am. Chem. Soc.*, 2009, **131**, 890–891; (*d*) G. Ciofani, S. Danti, G. G. Genchi, B. Mazzolai and V. Mattoli, *Small*, 2013, **9**, 1672–1685.
18 Q. Weng, X. Wang, X. Wang, Y. Bando and D. Golberg, *Chem. Soc. Rev.*, 2016, **45**, 3989–4012.
19 A. El Kadib, N. Wrońska, K. Lisowska, A. Anouar, N. Katir, K. Miłowska, B. Bielska and M. Bryszewska, *Functional Materials in Biomedical Applications*, Jenny Stanford Publishing, 2023, pp. 1–50.
20 N. Hammi, N. Wrońska, N. Katir, K. Lisowska, N. Marcotte, T. Cacciaguerra, M. Bryszewska and A. El Kadib, *ACS Appl. Bio Mater.*, 2019, **2**, 61–69.
21 (*a*) S. Frindy, A. Primo, A. E. K. Qaiss, R. Bouhfid, M. Lahcini, H. Garcia, M. Bousmina and A. El Kadib, *Carbohydr. Polym.*, 2016, **146**, 353–361; (*b*) J. Chabbi, O. Jennah, N. Katir, M. Lahcini, M. Bousmina and A. El Kadib, *Carbohydr. Polym.*, 2018, **183**, 287–293.
22 (*a*) S. Frindy, A. Primo, H. Ennajih, A. El Kacem Qaiss, R. Bouhfid, M. Lahcini, E. M. Essassi, H. Garcia and A. El Kadib, *Carbohydr. Polym.*, 2017, **167**, 297–305; (*b*) J. Chabbi, A. Aqil, N. Katir, B. Vertruyen, C. Jerôme, M. Lahcini and A. El Kadib, *Carbohydr. Polym.*, 2020, **230**, 115634.
23 N. Hammi, S. El Hankari, N. Katir, N. Marcotte, K. Draoui, S. Royer and A. El Kadib, *Microporous Mesoporous Mater.*, 2020, **306**, 110429.
24 S. Blilid, M. Kędzierska, K. Miłowska, N. Wrońska, M. El Achaby, N. Katir, E. Belamie, B. Alonso, K. Lisowska, M. Lahcini, M. Bryszewska and A. El Kadib, *ACS Sustainable Chem. Eng.*, 2020, **8**, 18354–18365.
25 N. Hammi, S. Chen, A. Primo, S. Royer, H. Garcia and A. El Kadib, *Green Chem.*, 2022, **24**, 4533–4543.
26 A. Mukheem, S. Shahabuddin, N. Akbar, A. Miskon, N. Muhamad Sarih, K. Sudesh, N. Ahmed Khan, R. Saidur and N. Sridewi, *Nanomaterials*, 2019, **9**, 645.
27 L. Durai, P. Yadav, H. Pant, V. V. S. S. Srikanth and S. Badhulika, *New J. Chem.*, 2020, **44**, 15919–15927.
28 (*a*) K. Behera, M. Kumari, Y.-H. Chang and F.-C. Chiu, *Int. J. Biol. Macromol.*, 2021, **186**, 135–144; (*b*) J. Chen, J. Shang, F. Xue, Q. Wei, N. Xu and E. Ding, *J. Polym. Res.*, 2019, **26**, 264.
29 S. Blilid, M. Boundor, N. Katir, M. El Achaby, M. Lahcini, J. P. Majoral, M. Bousmina and A. El Kadib, *Macromolecules*, 2023, **56**, 1223–1235.
30 L. L. Hu, L. W. Xiong and T. X. Yu, *Int. J. Mech. Sci.*, 2019, **159**, 116–125.
31 J. Chen, X. Liu, X. L. Zeng, H. Y. Ye and G. Q. Zhang, *Compos. Commun.*, 2022, **29**, 101038.
32 N. Wrońska, A. Anouar, M. El Achaby, K. Zawadzka, M. Kędzierska, K. Miłowska, N. Katir, K. Draoui, S. Różalska and I. Piwoński, *Materials*, 2020, **13**, 998.
33 N. Wrońska, N. Katir, K. Miłowska, N. Hammi, M. Nowak, M. Kędzierska, A. Anouar, K. Zawadzka, M. Bryszewska, A. El Kadib and K. Lisowska, *Int. J. Mol. Sci.*, 2021, **22**, 5839.
34 D. Raafat and H.-G. Sahl, *Microb. Biotechnol.*, 2009, **2**, 186–201.
35 X. Liu, L. Chang, L. Peng, R. Bai, Y. Wei, C. Ma and H. Liu, *ACS Appl. Mater. Interfaces*, 2021, **13**, 48358–48364.
36 (*a*) A. Merlo, V. R. S. S. Mokkapati, S. Pandit and I. Mijakovic, *Biomater. Sci.*, 2018, **6**, 2298–2311; (*b*) C. Parra, F. Montero-Silva, R. Henríquez, M. Flores, C. Garín, C. Ramírez, M. Moreno, J. Correa, M. Seeger and P. Häberle, *ACS Appl. Mater. Interfaces*, 2015, **7**, 6430–6437.
37 A. Raval, N. S. Yadav, S. Narwani, K. Somkuwar, V. Verma, H. Almubarak, S. M. Alqahtani, R. Tasleem, A. M. Luke, S. T. Kuriadom and M. I. Karobari, *J. Funct. Biomater.*, 2023, **14**, 201.
38 S. Mateti, C. S. Wong, Z. Liu, W. Yang, Y. Li, L. H. Li and Y. Chen, *Nano Res.*, 2018, **11**, 334–342.
39 B. Poljsak, D. Šuput and I. Milisav, *Oxid. Med. Cell Longev.*, 2013, **2013**, 956792.
40 K. Kuroda, G. A. Caputo and W. F. DeGrado, *Eur. J. Chem.*, 2009, **15**, 1123–1133.
41 X. Xie, Z. Hou, G. Duan, S. Zhang, H. Zhou, Z. Yang and R. Zhou, *Colloids Surf., B*, 2021, **203**, 111765.
42 (*a*) A. Wan, Q. Xu, Y. Sun and H. Li, *J. Agric. Food Chem.*, 2013, **61**, 6921–6928; (*b*) T. Sun, D. Zhou, J. Xie and F. Mao, *Eur. Food Res. Technol.*, 2007, **225**, 451–456; (*c*) P. Ahmad, A. Khalid, M. U. Khandaker, F. Rehman, M. I. Khan, H. Ali, N. Muhammad, M. S. Kiyani, A. Sulieman, M. A. Rauf Khan, Z. Razzaq, A. Khan, S. Haq, Y. Saeed and M. I. Irshad, *Mater. Sci. Semicond. Process.*, 2022, **141**, 106419.